

# Journal of Materials Chemistry A

Materials for energy and sustainability

Accepted Manuscript

This article can be cited before page numbers have been issued, to do this please use: A. B. Jorge, G. Tian, R. Jervis, J. Briscoe and M. Titirici, *J. Mater. Chem. A*, 2022, DOI: 10.1039/D2TA00739H.



This is an Accepted Manuscript, which has been through the Royal Society of Chemistry peer review process and has been accepted for publication.

Accepted Manuscripts are published online shortly after acceptance, before technical editing, formatting and proof reading. Using this free service, authors can make their results available to the community, in citable form, before we publish the edited article. We will replace this Accepted Manuscript with the edited and formatted Advance Article as soon as it is available.

You can find more information about Accepted Manuscripts in the [Information for Authors](#).

Please note that technical editing may introduce minor changes to the text and/or graphics, which may alter content. The journal's standard [Terms & Conditions](#) and the [Ethical guidelines](#) still apply. In no event shall the Royal Society of Chemistry be held responsible for any errors or omissions in this Accepted Manuscript or any consequences arising from the use of any information it contains.

## ARTICLE

# Efficient Harvesting and Storage of Solar Energy of an All-Vanadium Solar Redox Flow Battery with a MoS<sub>2</sub>@TiO<sub>2</sub> Photoelectrode

Gengyu Tian,<sup>a</sup> Rhodri Jervis,<sup>b</sup> Joe Briscoe,<sup>a</sup> Magdalena Titirici<sup>c</sup> and Ana Jorge Sobrido\*<sup>a</sup>

Received 00th January 20xx,  
Accepted 00th January 20xx

DOI: 10.1039/x0xx00000x

Solar redox flow batteries constitute an emerging technology that provide a smart alternative for the capture and storage of discontinuous solar energy through the photo-generation of the discharged redox species employed in traditional redox flow batteries. Here, we show that a MoS<sub>2</sub>-decorated TiO<sub>2</sub> (MoS<sub>2</sub>@TiO<sub>2</sub>) photoelectrode can successfully harvest light to be stored in a solar redox flow battery using vanadium ions as redox active species in both catholyte and anolyte, and without the use of any bias. MoS<sub>2</sub>@TiO<sub>2</sub> photoelectrode achieved an average photocurrent density of ~0.4 mA cm<sup>-2</sup> versus 0.08 mA cm<sup>-2</sup> for bare TiO<sub>2</sub>, when tested for the oxidation of V<sup>4+</sup> to V<sup>5+</sup>, attributed to a more efficient light harvesting and charge separation for the MoS<sub>2</sub>@TiO<sub>2</sub> relative to TiO<sub>2</sub>. The designed solar redox flow cell exhibited an optimal overall solar-to-output energy conversion efficiency (SOEE) of ~4.78%, which outperforms previously reported solar redox flow batteries. This work demonstrates the potential of MoS<sub>2</sub>@TiO<sub>2</sub> photoelectrode to efficiently convert solar energy in to chemical energy in a solar redox flow battery, and it also validates the great potential of this technology to increase reliability in renewable energies.

## Introduction

The direct storage of sunlight in the form of hydrogen *via* overall water splitting using photoelectrochemical cells (PECs) has been the subject of extensive research in the last few decades.<sup>1-4</sup> The main benefit of this technology is the clean production of hydrogen through the use of solar energy.<sup>5,6</sup> However, the sluggish kinetics of water splitting, particularly the oxygen evolution reaction, the low overall energy conversion efficiency, and the high cost of transportation and storage of hydrogen have somewhat slowed down the take-off of the hydrogen economy.<sup>7,8</sup> Because of this, researchers are increasingly shifting their efforts towards the development of alternative technologies that can offer faster chemical reaction kinetics to store solar energy. Among them, solar redox flow batteries (SRFBs) have attracted recent attention. SRFBs are hybrids between PECs and redox flow batteries (RFBs). They use renewable light energy to charge redox substances and solar energy in the form of chemical energy.<sup>9-16</sup> One example of recent developments in this area is the SRFB designed by Yangen *et al.* that used I<sup>3-</sup>/I<sup>-</sup> and Br<sup>-</sup>/Br<sup>3-</sup> as redox active pairs.<sup>17</sup> The SRFB was driven by a WO<sub>3</sub>-decorated BiVO<sub>4</sub> photoanode and provided 1.25% solar-output energy conversion efficiency.

Yan *et al.* reported a SRFB consisting of a Li<sub>2</sub>WO<sub>4</sub>/LiI redox couple and a dye-sensitised TiO<sub>2</sub> photoelectrode, enabling a battery capacity of 0.0195 mA h mL<sup>-1</sup> at a discharge density of 0.075 mA·cm<sup>-2</sup>.<sup>1</sup> Recently, Amirreza *et al.* built a tandem with a bare hematite photoanode and two dye-sensitised solar cells connected in series<sup>2</sup>; the conversion efficiency from solar to chemical energy of the AQDS (anthraquinone-2,7-disulfonate) / iodide SRFB using only hematite as the photoanode was about 0.1%.

Due to its high reversibility and fast react kinetics, all-vanadium redox flow batteries have been widely researched and developed around the world<sup>3-6</sup>, including vanadium-based SRFBs, too. Hao *et al.* applied a nitrogen-doped TiO<sub>2</sub> photoanode to a microfluidic all-vanadium photoelectrochemical cell with average photocurrent density of 0.1 mA cm<sup>-2</sup>.<sup>7</sup> Zi *et al.* demonstrated an AQDS/V<sup>4+</sup> SRFB able to generate a relatively stable photocurrent of 0.14 mA cm<sup>-2</sup> using TiO<sub>2</sub> nanoparticles supported on fluorine-doped tin oxide (FTO) as photoanode.<sup>8</sup> Titanium dioxide (TiO<sub>2</sub>) has been extensively investigated as a photocatalyst since the discovery of its unique properties in 1972, including remarkable stability against photocorrosion and wide band gap, large enough to provide sufficient energy to drive a variety of useful reactions.<sup>9-12</sup> Although the stability of TiO<sub>2</sub> is excellent, the lack of visible light absorption along with the rapid recombination of photogenerated electron-hole pairs produced usually results in low quantum efficiency and poor photocatalytic activity<sup>13</sup>. Multiple strategies to improve the photocatalytic performance of TiO<sub>2</sub> have been explored, including doping with different elements<sup>7, 14, 15</sup>, decorating with noble metals<sup>16, 17</sup>, and

<sup>a</sup> School of Engineering and Materials Science, Queen Mary University of London, E1 4NS, United Kingdom.

<sup>b</sup> Electrochemical Innovation Lab, Department of Chemical Engineering, University College London, WC1E 7JE, United Kingdom.

<sup>c</sup> Department of Chemical Engineering, Imperial College London, South Kensington Campus, SW7 2AZ, United Kingdom.

Electronic Supplementary Information (ESI) available: [details of any supplementary information available should be included here]. See DOI: 10.1039/x0xx00000x



engineering heterojunctions with other semiconductors<sup>18, 19</sup>. Coupling TiO<sub>2</sub> with other semiconductors to form heterojunctions is an effective way to boost the performance of TiO<sub>2</sub><sup>20, 21</sup> via bending of the photoelectrode band structure, which in turn provides an easier transfer path for the photogenerated electrons and holes and enables a more efficient process<sup>22, 23</sup>. In addition, the design of a heterojunction with a semiconductor of smaller band gap provides a pathway to utilise the visible region of the solar spectrum, increasing the overall efficiency<sup>24, 25</sup>. Some reported examples of such systems include Cu<sub>2</sub>O@TiO<sub>2</sub><sup>26</sup>, g-C<sub>3</sub>N<sub>4</sub>@TiO<sub>2</sub><sup>27</sup> and MoS<sub>2</sub>@TiO<sub>2</sub><sup>28, 29</sup>.

Here we present for the first time a SRFB with exceptional solar-to-output energy conversion efficiency (SOEE), consisting of a MoS<sub>2</sub>@TiO<sub>2</sub> photoelectrode (photoanode) and carbon felt as counter electrode (cathode). Specifically, we have studied the redox pairs V<sup>5+</sup>/V<sup>4+</sup> and V<sup>4+</sup>/V<sup>3+</sup>, which redox potentials match the band gap of the photoelectrode heterojunction. We synthesised the MoS<sub>2</sub>@TiO<sub>2</sub> thin films supported on FTO glass substrate via a hydrothermal route. The deposition of MoS<sub>2</sub> decorated TiO<sub>2</sub> ensured an increased specific surface area and effective light response, which translated into an enhanced photon capturing and charge transfer. When sunlight reaches the photoelectrode, the photogenerated holes oxidize V<sup>4+</sup> to V<sup>5+</sup> at the interface between photoelectrode and anolyte, while the photogenerated electrons reduce V<sup>4+</sup> to V<sup>3+</sup> at the interface between carbon felt and catholyte. Thus, the oxidized and reduced forms of V<sup>4+</sup>, V<sup>5+</sup> and V<sup>3+</sup>, respectively, retain the chemical energy that can be converted to electricity via the reverse reaction (Figure 1). This SRFB can be written as TiO<sub>2</sub>/MoS<sub>2</sub>(s)|V<sup>4+</sup>, V<sup>5+</sup>||V<sup>4+</sup>, V<sup>3+</sup>|carbon. The developed system provides ~0.4 mA cm<sup>-2</sup> photocurrent which is higher than the similar TiO<sub>2</sub>-based all-vanadium systems with acidic electrolytes<sup>7, 8</sup>. This is the first time that the MoS<sub>2</sub>@TiO<sub>2</sub> photoelectrode has shown good catalytic activity for vanadium redox couples, with an overall SOEE of 4.78%, remarkably higher than previously reported SRFB systems (Table S1, Supporting Information).<sup>30, 31</sup>

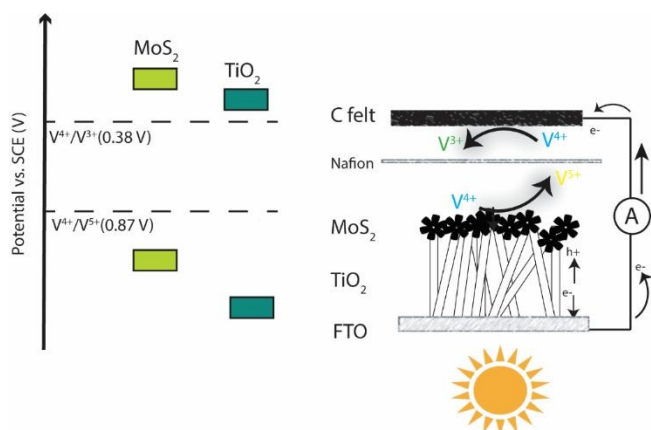


**Figure 1.** Schematic representation of the SRFB system studied in this work.

## Experimental

### Material preparation

Preparation of TiO<sub>2</sub> nanorod arrays. TiO<sub>2</sub> nanorod arrays (NRs) on FTO were prepared using a hydrothermal method reported elsewhere<sup>32</sup>. Briefly, 60 mL deionised water was mixed with 30 mL of concentrated hydrochloric acid (36.5% by weight), and the solution was sonicated for 15 min. Then, 0.1, 0.3, or 0.5 mL of titanium (IV) butoxide (purum, ≥ 97%, gravimetric, Sigma) were added to the solution and sonicated for further 15 min. The FTO substrates were placed into the Teflon liner (200 mL). The hydrothermal synthesis was conducted at 180 °C for 12 h. The resultant sample was rinsed extensively with deionised water, then dried at 80 °C for 1 h and thermally treated at 500 °C in air for 1 h.

### Fabrication of MoS<sub>2</sub> nanoflowers onto TiO<sub>2</sub> NRs (MoS<sub>2</sub>@TiO<sub>2</sub>).

MoS<sub>2</sub> nanoflowers were grown onto the TiO<sub>2</sub> NRs (0.1/0.3/0.5 mL) by a facile hydrothermal reaction<sup>28</sup>. Firstly, 242 mg (0.001 mol) Na<sub>2</sub>MoO<sub>4</sub>·2H<sub>2</sub>O powder (99%, Sigma) and 242 mg (0.002 mol) L-Cysteine (99.99%, Sigma) were mixed in 90 mL deionised water under magnetic stirring for 10 min, then transferred to a Teflon-lined autoclave and stirred for additional 5 min. Subsequently, the TiO<sub>2</sub> NRs previously prepared were placed into the autoclave containing the MoS<sub>2</sub> precursors. The hydrothermal synthesis and deposition of MoS<sub>2</sub> onto the TiO<sub>2</sub> NRs were conducted at 200 °C for 12 h, followed by rinsing with deionized water and drying at 80 °C for 1 h. The resultant samples were labelled as MoS<sub>2</sub>@TiO<sub>2</sub>-0.1, MoS<sub>2</sub>@TiO<sub>2</sub>-0.3 and MoS<sub>2</sub>@TiO<sub>2</sub>-0.5.

### Characterisation

The morphology and microstructure of the prepared photoelectrodes were characterised using a field-emission scanning electron microscope (FESEM, Philips FEI Quanta 200 FEG) equipped with an energy dispersive X-ray spectrometer (EDS, operating at an accelerating voltage of 30 kV). The crystal phases of samples were determined by X-ray diffraction (XRD) with Panalytical Xpert Pro diffractometer using Cu Kα radiation source (1.5418 Å). The optical absorption properties were determined by using a UV-vis spectrophotometer (Lambda 950, PerkinElmer) equipped with an integrating sphere (PerkinElmer) within a wavelength range of 350 to 800 nm and a step of 1 nm. The surface chemical states of photocatalysts were analysed by X-ray photoelectron spectroscopy (XPS, Thermo Fisher Nexsa X-ray spectrometer, Al Kα monochromatic X-ray source). ICP-MS analysis was performed using a Microwave Plasma Atomic Emission Spectroscopy (4210 MP-AES).

### Electrochemical and photoelectrochemical characterisation

A three-electrode electrochemical cell was employed to study the electrochemical behaviour of the carbon felt electrode against vanadium ion species. The carbon felts (3.18 mm thick, 99.0% Alfa Aesar) were pre-treated in a MTI 1200x tubular furnace at 800 °C for 2 h, using a heating rate of 3 °C min<sup>-1</sup> and a nitrogen flow rate of 0.5 l min<sup>-1</sup>.<sup>33</sup> The size of the carbon felt electrodes was 1.0 cm<sup>2</sup> (0.32 cm<sup>3</sup>). KCl saturated calomel Hg<sub>2</sub>Cl<sub>2</sub>



electrode (SCE) and Pt foil were employed as reference and counter electrodes, respectively. Cyclic voltammetry (CV) experiments were conducted between -1.0 and 1.6 V *versus* SCE, at a scan rate of 10 mV s<sup>-1</sup>, and electrolyte with a concentration in 0.1 M or 1.0 M V<sup>4+</sup> (vanadium IV oxide sulfate hydrate, Sigma-Aldrich, 97%) and 1.0, 2.0 or 3.0 M H<sub>2</sub>SO<sub>4</sub> (Sigma, 98%). Electrochemical impedance spectroscopy (EIS) experiments were conducted using a frequency range of 0.1 MHz to 0.1 Hz and a perturbation of 10 mV. All the electrochemical experiments were carried out using a potentiostat Gamry IFC5000-05520.

Photoelectrochemical studies were conducted in a three-electrode electrochemical cell using TiO<sub>2</sub> or MoS<sub>2</sub>@TiO<sub>2</sub> as working electrode, and SCE and Pt foil as reference and counter electrodes, respectively. 0.1 M and 1.0 M V<sup>4+</sup> in 3.0 M H<sub>2</sub>SO<sub>4</sub> were used as the electrolyte. Linear sweep voltammetry (LSV) measurements were conducted at a scan rate of 10 mV s<sup>-1</sup> in the voltage range of -0.5 V to 0.5 V vs. SCE. EIS photoelectrochemical experiments were also conducted at frequency range of 0.1 MHz to 0.1 Hz and 10 mV perturbation. The illuminated area (back illumination) of the working electrode was 1.0 cm<sup>2</sup>. The photoelectrode was irradiated by simulated solar light (400 W Xe lamp) using an AM 1.5 G filter. The power density of the incident light was calibrated to 100 mW cm<sup>-2</sup> by using an optical power meter with silicon photodetector (Newport 818-SL) as a certified reference. The illuminated area of the working electrode was 1.0 cm<sup>2</sup>.

### Redox flow battery testing

Charge-discharge experiments were conducted in the voltage range 0 to 1.1 V using a current density of 1.0 mA cm<sup>-2</sup> with 1.0 M V<sup>4+</sup>. The electrolyte was pre-discharged to 0 V at current density of 0.1 mA cm<sup>-2</sup>. Carbon felts separated by a Nafion<sup>®</sup> membrane were used as positive and negative electrodes. The discharge current density after photocharge is 0.4 mA cm<sup>-2</sup>. The carbon felts underwent the same thermal treatment described in the electrochemical characterisation section. The Nafion membrane (115, 0.005 in. Thick, DuPont de Nemours & Co) was subjected to the following treatment prior to their use: firstly, immersed in 50 mL 5 wt.% H<sub>2</sub>O<sub>2</sub> 80 °C 1 h, followed by an hour treatment at 80 °C in distilled water, and another hour at 80 °C in 1.0 M H<sub>2</sub>SO<sub>4</sub>. The membrane was finally treated at 80 °C for 1h in distilled water. A volume of 20 mL was employed as initial catholyte and anolyte, respectively. The experiment was carried out using a peristaltic pump with double head to control the flow of electrolyte on both sides of the redox flow cell to 2.5 mL min<sup>-1</sup>. The size of carbon felt as working electrode for redox flow battery testing is 5.0 cm<sup>2</sup> (1.59cm<sup>3</sup>).

### Solar flow battery testing

The SRFB consisted of a modified redox flow battery (**Figure S1a, Supporting Information**), with a window in the anolyte side to enable the irradiation of the photoanode with the Xe lamp light source, and a redox flow battery (**Figure S1b, Supporting Information**), coupled to two electrolyte tanks and a peristaltic pump. All electrochemical data were collected

using a Gamry IFC5000-05520 potentiostat. The solar flow cell assembly included the MoS<sub>2</sub>@TiO<sub>2</sub> photoelectrode and carbon felt, separated by a Nafion<sup>®</sup> membrane. Both carbon felts and Nafion<sup>®</sup> membrane were pretreated as explained in the previous section. Photocharging of the SRFB was conducted without any external bias through irradiation of the photoanode using simulated solar light (400 W Xe lamp) using an AM 1.5 G filter. As the SRFB photocharges, the V<sup>4+</sup> present oxidises to V<sup>5+</sup> in the anolyte and reduces to V<sup>3+</sup> in the catholyte. EIS studies of MoS<sub>2</sub>@TiO<sub>2</sub>-0.5 were conducted in SRFB configuration, using 1.0 M V<sup>4+</sup> in 3.0 M H<sub>2</sub>SO<sub>4</sub>, frequency range 0.1 MHz - 0.1 Hz and perturbation of 10 mV. The illuminated area of the working electrode in the solar flow cell was 5.0 cm<sup>2</sup>.

## Results and discussion

Three TiO<sub>2</sub> thin films were synthesised using different amounts of titanium (IV) butoxide (0.1, 0.3 and 0.5 mL) and deposited onto FTO using a hydrothermal route. The TiO<sub>2</sub> films (**Figure 2**) displayed a rod-like morphology typically observed in the literature<sup>36</sup> with a crystal structure corresponding to rutile, as determined by x-ray diffraction (**Figure S2, Supporting Information**).

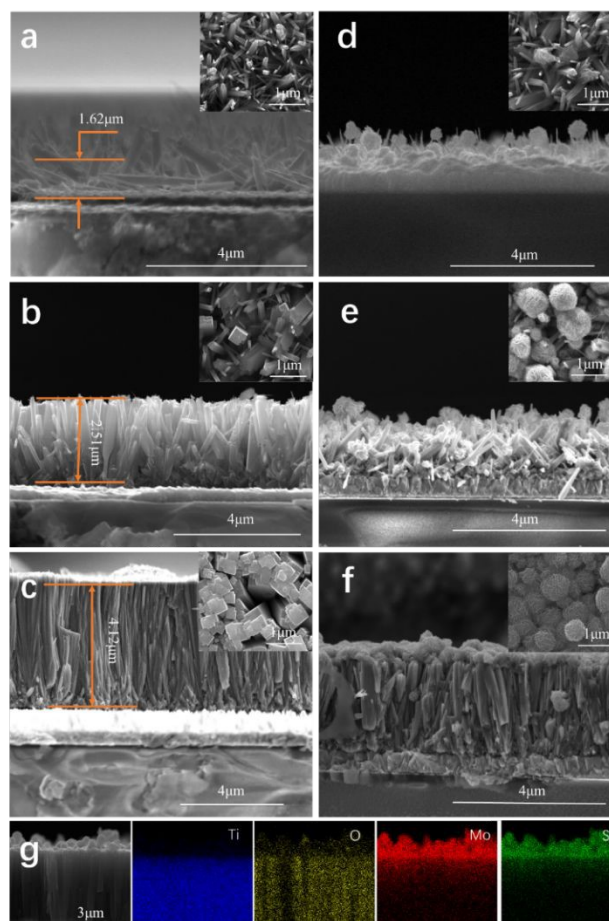


**Figure 2.** SEM images of TiO<sub>2</sub> thin films obtained using (a) TiO<sub>2</sub>-0.1, (b) TiO<sub>2</sub>-0.3 and (c) TiO<sub>2</sub>-0.5. (d) MoS<sub>2</sub>@TiO<sub>2</sub>-0.1, (e) MoS<sub>2</sub>@TiO<sub>2</sub>-0.3 and (f) MoS<sub>2</sub>@TiO<sub>2</sub>-0.5; (g) EDS of MoS<sub>2</sub>@TiO<sub>2</sub>-0.5.



The TiO<sub>2</sub> rods became larger with increasing the amount of titanium (IV) butoxide. The TiO<sub>2</sub> rods produced using 0.1 mL of precursor were relatively short (~1.6 μm) and randomly oriented (**Figure 2a**). As the amount of precursor is increased to 0.3 mL, generally the TiO<sub>2</sub> rods thicken and their length increased by almost 1 μm, to ~2.5 μm (**Figure 2b**). However, in this case, size, length, and orientation of the rods was still inhomogeneous. As the amount of titanium (IV) butoxide was further increased to 0.5 mL, the TiO<sub>2</sub> rods became much thicker (4.12 μm). Moreover, the orientation and size of the rods tended to be more uniform (**Figure 2c**). The film itself also grew into a denser more compacted layer with additional titanium (IV) butoxide.

MoS<sub>2</sub> nanoflowers were grown onto the three TiO<sub>2</sub> films prepared. In the case of the MoS<sub>2</sub>@TiO<sub>2</sub>-0.1 film, only a small amount of MoS<sub>2</sub> deposited onto the TiO<sub>2</sub> rods, and also in the space between rods (**Figure 2d**). The synthesis and growth of MoS<sub>2</sub> onto TiO<sub>2</sub> with a tighter surface structure (MoS<sub>2</sub>@TiO<sub>2</sub>-0.3 and MoS<sub>2</sub>@TiO<sub>2</sub>-0.5) prevented the MoS<sub>2</sub> nanoflowers from depositing into the space between TiO<sub>2</sub> rods, leading to the formation of more uniform MoS<sub>2</sub> layers (**Figure 2e, f**). A higher magnification of the MoS<sub>2</sub> nanoflowers on the upper right corner of **Figure 2f**, showed that each MoS<sub>2</sub> nanoflower had a diameter of ~500 nm and exhibited > 100 sheets. According to literature, the higher the number of layers of MoS<sub>2</sub> nanosheets, the higher the photocatalytic performance, as more nanosheets will provide more active sites and area for the reaction<sup>32, 34, 35</sup>. EDS data (**Figure 2g** and **Figure S3, Supporting Information**) for MoS<sub>2</sub>@TiO<sub>2</sub>-0.5 material supported the SEM data.

The UV-vis absorption spectra of TiO<sub>2</sub> and MoS<sub>2</sub>@TiO<sub>2</sub> photoelectrodes in front illumination mode (**Figure 3a**) showed the increase in light absorption within the visible range for the samples containing MoS<sub>2</sub>, as expected. The back illumination spectra (**Figure S4, Supporting Information**) displayed similar behaviour with additional features due to interference in the case of MoS<sub>2</sub>@TiO<sub>2</sub> photoelectrodes, although some reports have suggested that the additional bands observed may be due to MoS<sub>2</sub><sup>25-30</sup>. XPS was used to analyse the oxidation state and electronic environment of Ti, Mo, S and O. The Ti 2p line XPS spectrum for TiO<sub>2</sub>-0.5 (**Figure 3b**) confirmed that the surface of TiO<sub>2</sub> mainly consists of Ti<sup>4+</sup> 2p<sub>1/2</sub>, Ti<sup>4+</sup> 2p<sub>3/2</sub>, Ti-O bond and O-H bond as expected for TiO<sub>2</sub>, with binding energies of 465.1 eV, 459.4 eV, and 530.6 eV and 532.3 eV, respectively<sup>32</sup>. In **Figure 3c, d**, the Mo 3d and S 2p line XPS spectra for MoS<sub>2</sub>@TiO<sub>2</sub>-0.5 are shown, respectively. The Mo 3d line XPS spectrum indicated the existence of two different states of MoS<sub>2</sub>: 1T-MoS<sub>2</sub> and 2H-MoS<sub>2</sub>, both with Mo<sup>4+</sup> as the dominant oxidation state. Previous research has indicated that Mo 3d and S 2p XPS signals of the 1T-MoS<sub>2</sub> phase exhibit a higher binding energy (about 1 eV) than the corresponding signals for 2H-MoS<sub>2</sub><sup>36</sup>. The 2H and 1T phases exhibited binding energies of 229.4 and 232.2 eV for 3d<sub>1/2</sub> and 3d<sub>3/2</sub>, respectively for 2H-MoS<sub>2</sub> and of 228.1 and 231.3 eV for 3d<sub>5/2</sub> and 3d<sub>3/2</sub>, respectively for 1T-MoS<sub>2</sub><sup>37</sup>. Two small features at 235.2 eV (Mo 3d<sub>3/2</sub>) and 233.6 eV (Mo 3d<sub>5/2</sub>) attributed to Mo<sup>6+</sup> from some MoO<sub>3</sub> formed at the surface were

also observed<sup>38, 39</sup>. A clear peak corresponding to S 2s at 225.5 eV could also be detected. The S 2p line (**Figure 3d**) exhibited two doublets corresponding to 2p<sub>1/2</sub> and 2p<sub>3/2</sub> at binding energies of 163.2 eV and 161.4 eV, respectively<sup>40</sup>. Additionally, peak contributions corresponding to bridging disulfides found in 1T-MoS<sub>2</sub> were observed at 162.3 eV for 2p<sub>1/2</sub> and at 160.9 eV for 2p<sub>3/2</sub><sup>41</sup>. The XPS survey spectra corresponding to TiO<sub>2</sub>-0.5 and MoS<sub>2</sub>@TiO<sub>2</sub>-0.5 and the XPS O 1s line for MoS<sub>2</sub>@TiO<sub>2</sub>-0.5 are shown in **Figure S5, Supporting Information**.

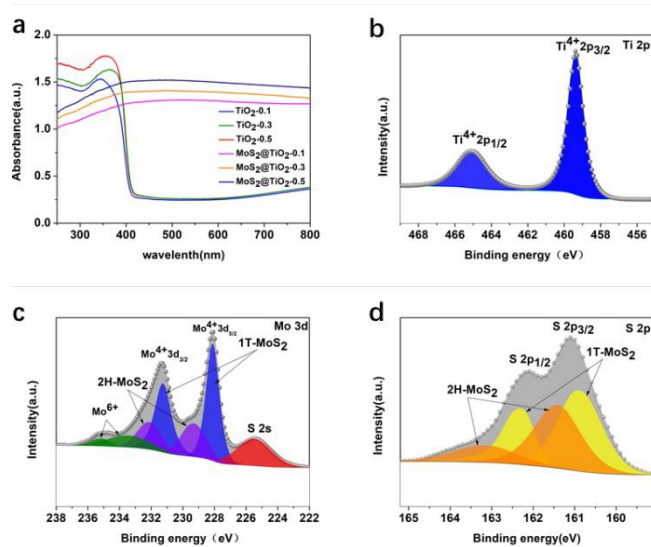


**Figure 3.** UV-vis spectra of TiO<sub>2</sub>-0.5 and MoS<sub>2</sub>@TiO<sub>2</sub>-0.5 using (a) front-illumination mode, XPS spectra of (b) Ti 2p from TiO<sub>2</sub>-0.5, and XPS spectra of (c) Mo 3d, (d) S 2p from MoS<sub>2</sub>@TiO<sub>2</sub>-0.5

To study the influence of the electrolyte on the performance of the system, a CV experiment using carbon felt as working electrode with 1.0M/2.0M/3.0M sulfuric acid (without any V species) was conducted (**Figure S6, Supporting Information**). The results showed that the ionic conductivity increased with increasing the concentration of sulfuric acid. CV and EIS of 0.1 M V<sup>4+</sup> in different sulfuric acid concentrations were also conducted in a three-electrode electrochemical cell configuration (**Figure S7, Supporting Information**). The results suggested that a higher concentration of H<sub>2</sub>SO<sub>4</sub> facilitates the electrochemical reaction, resulting in more reversible redox processes at the highest concentration, 3.0 M H<sub>2</sub>SO<sub>4</sub>. The EIS result in **Figures S7c and d** confirmed that higher concentration of sulfuric acid as electrolyte can decrease the resistance through increasing the ionic conductivity of the electrolyte. The CV result indicated a redox potential difference between 0.1 M V<sup>3+</sup>/V<sup>4+</sup> and V<sup>4+</sup>/V<sup>5+</sup> of ~0.49 V in 3.0 M H<sub>2</sub>SO<sub>4</sub> using thermally treated carbon felt as the working electrode (**Figure 4a**). There exists a reduction peak corresponding to V<sup>3+</sup>/V<sup>2+</sup>; however, no oxidation peak V<sup>2+</sup> to V<sup>3+</sup> was observed. This has been previously reported in the literature, due to the extremely easy oxidation of V<sup>2+</sup> in air.<sup>42,43</sup> In order to match the photocurrent density, 1.0 mA cm<sup>-2</sup> was selected as the charge and discharge current density to test the reversibility and stability of the V<sup>3+</sup>/V<sup>4+</sup> and V<sup>4+</sup>/V<sup>5+</sup> redox pairs. The redox flow cell assembled with the



same carbon felts and redox pairs exhibited a good reversibility upon charge and discharge cycling (Figure 4b) with an average capacity of  $1077 \text{ mAh L}^{-1}$  and coulombic efficiency of 99.2% at a current density of  $1.0 \text{ mA cm}^{-2}$  within 25 cycles (Figure 4c).

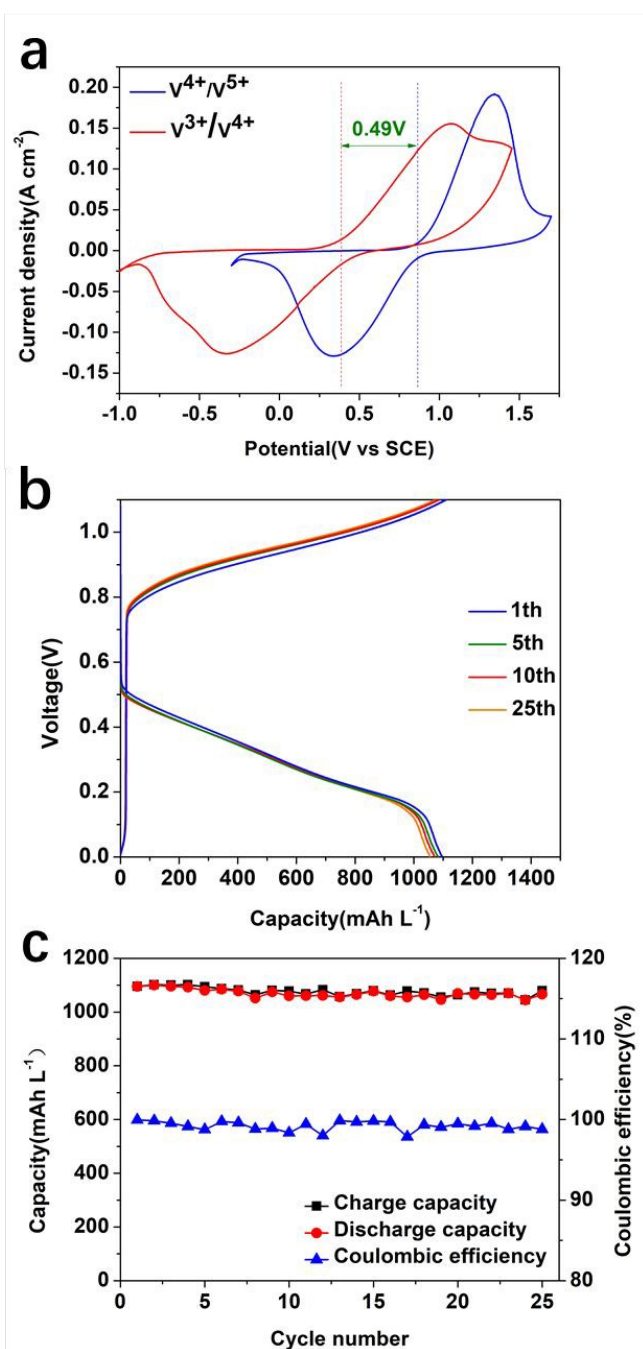
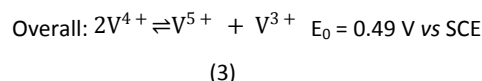
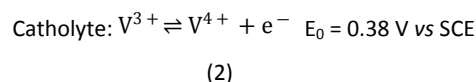
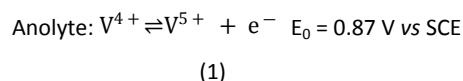


**Figure 4.** (a) CV in  $0.1 \text{ M V}^{3+}/\text{V}^{4+}$  and  $\text{V}^{4+}/\text{V}^{5+}$ , with a three-electrode electrochemical cell using in  $3.0 \text{ M H}_2\text{SO}_4$ , carbon felt, SCE and a Pt coil as working, reference, and counter electrode, respectively. (b) Charge/discharge experiments for a redox flow cell using  $1.0 \text{ M V}^{4+}$ ,  $3.0 \text{ M H}_2\text{SO}_4$  electrolyte, current density of  $1.0 \text{ mA cm}^{-2}$  from  $0 \text{ V}$  to  $1.1 \text{ V}$ . (c) charge-discharge capacity and coulombic efficiency of the RFB.

The redox processes of  $\text{V}^{4+}/\text{V}^{5+}$  and  $\text{V}^{4+}/\text{V}^{3+}$  redox pairs in RFB can be summarised in Equation 1, 2, 3 as follows:



After testing the performance of the RFB using  $\text{V}^{3+}/\text{V}^{4+}$  and  $\text{V}^{4+}/\text{V}^{5+}$ , the electrochemical behaviour of the  $\text{TiO}_2$  and  $\text{MoS}_2/\text{TiO}_2$  photoanodes against  $\text{V}^{4+}$ . Figure 5a and 5b shows the LSV measurements in  $0.1 \text{ M}$  and  $1.0 \text{ M V}^{4+}$ , respectively, in  $3.0 \text{ M H}_2\text{SO}_4$  for  $\text{TiO}_2\text{-}0.5$  and  $\text{MoS}_2/\text{TiO}_2\text{-}0.5$ . The  $\text{MoS}_2/\text{TiO}_2$  photoelectrode exhibited much higher performance than  $\text{TiO}_2\text{-}0.5$ , being able to achieve a photovoltage of  $\sim 450 \text{ mV vs SCE}$ , about  $\sim 100 \text{ mV}$  higher than the  $\text{TiO}_2\text{-}0.5$  photoelectrode for both  $\text{V}^{4+}$  concentrations. Upon applying potential bias, there is an expected increase in photocurrent for both photoelectrodes, which is also more noticeable in the case of  $\text{MoS}_2/\text{TiO}_2\text{-}0.5$ . In the case of the  $\text{MoS}_2/\text{TiO}_2\text{-}0.5$ , the increase rate is faster for the more concentrated  $\text{V}^{4+}$  electrolyte ( $1.0 \text{ M}$ ), reaching  $0.6 \text{ mA cm}^{-2}$  compared to  $\sim 0.4 \text{ mA cm}^{-2}$  for  $0.1 \text{ M V}^{4+}$  at  $0.4 \text{ V vs SCE}$ . Interestingly, there was no significant effect on the photocurrent response when increasing the  $\text{V}^{4+}$  concentration for the  $\text{TiO}_2\text{-}0.5$  photoelectrode when applying bias. We attribute this to the fact that the  $\text{TiO}_2$  photoelectrode is already performing as its maximum capacity, in terms of the holes that can produce at a given time, so a higher concentration of  $\text{V}^{4+}$  would not change the number of holes that can reach to the interface of electrolyte/ $\text{TiO}_2$ .

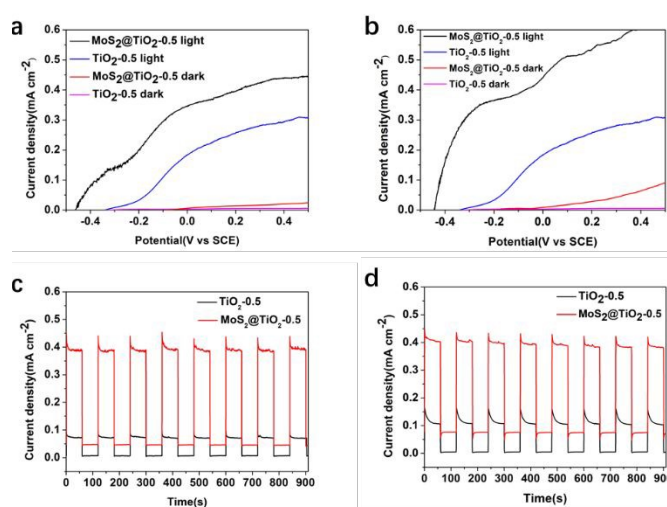


**Figure 5.** LSV in (a)  $0.1 \text{ M V}^{4+}$  and (b)  $1.0 \text{ M V}^{4+}$  with a three-electrode electrochemical cell using in  $3.0 \text{ M H}_2\text{SO}_4$ , SCE and a Pt coil as reference and counter electrode, respectively. Chopped-



chronoamperometry experiment for a SRFB using  $\text{TiO}_2\text{-}0.5$  or  $\text{MoS}_2\text{@TiO}_2\text{-}0.5$  as photoanodes and thermal treated carbon felt as cathode in (c) 0.1 M  $\text{V}^{4+}$  and (d) 1.0 M  $\text{V}^{4+}$  with 3.0 M  $\text{H}_2\text{SO}_4$  2.5 mL  $\text{min}^{-1}$  flow rate and light source 100  $\text{mW cm}^{-2}$  (AG1.5).

Chronoamperometric measurements of all the photoelectrodes ( $\text{TiO}_2\text{-}0.1$ ,  $\text{TiO}_2\text{-}0.3$ ,  $\text{TiO}_2\text{-}0.5$  and their  $\text{MoS}_2\text{@TiO}_2$  counterparts, **Figure S8, Supporting Information**) conducted in a SRFB configuration showed that the performance of the samples was much more affected by the densification level and thickness of the  $\text{TiO}_2$  layer than by the presence of  $\text{MoS}_2$  for the samples  $\text{TiO}_2\text{-}0.1$ ,  $\text{TiO}_2\text{-}0.3$ ,  $\text{MoS}_2\text{@TiO}_2\text{-}0.1$  and  $\text{MoS}_2\text{@TiO}_2\text{-}0.3$ , all of which exhibited a similar photocurrent response. This is likely due to a better alignment of the  $\text{TiO}_2$  rods for the more compact samples<sup>32</sup>,  $\text{TiO}_2\text{-}0.5$  and  $\text{MoS}_2\text{@TiO}_2\text{-}0.5$ . Therefore, a significant enhancement in the photoresponse when adding  $\text{MoS}_2$  was only observed for these more compact  $\text{TiO}_2$  layers, with the sample  $\text{MoS}_2\text{@TiO}_2\text{-}0.5$ , exhibiting 0.4  $\text{mA cm}^{-2}$  versus 0.08  $\text{mA cm}^{-2}$  for  $\text{TiO}_2\text{-}0.5$  in 0.1 M  $\text{V}^{4+}$ . Chopped-chronoamperometry experiments in 0.1 M (**Figure 5c**) and 1.0 M  $\text{V}^{4+}$  (**Figure 5d**), in 3.0 M  $\text{H}_2\text{SO}_4$  also revealed that the  $\text{MoS}_2\text{@TiO}_2\text{-}0.5$  photoanode presented a stable photocurrent density and quick photoresponse in  $\text{V}^{4+}$  flowing electrolyte.

A stability test was carried out for the best performing photoelectrode,  $\text{MoS}_2\text{@TiO}_2\text{-}0.5$  in 1.0 M  $\text{V}^{4+}$ , 3.0 M  $\text{H}_2\text{SO}_4$  electrolyte using a SRFB configuration. **Figure 6a** shows the photocharging process conducted for five cycles. As it can be observed, full photocharge was achieved in  $\sim 60$  min. As the number of charge/discharge cycles increased, the photocurrent density of  $\text{MoS}_2\text{@TiO}_2\text{-}0.5$  decreased. After each full photocharge and discharge, the photocurrent density decreased from  $\sim 0.4$   $\text{mA cm}^{-2}$  to 0.26  $\text{mA cm}^{-2}$  for the 5<sup>th</sup> cycle. This is attributed to the low stability of  $\text{MoS}_2$  under the harsh acidic working conditions and more studies to protect the  $\text{MoS}_2$  are currently being explored to mitigate this effect. The fluctuations observed in the charge profiles are due to the slow photocorrosion process affecting the  $\text{MoS}_2$  under the acidic working environment. When the photons inject into the  $\text{MoS}_2\text{@TiO}_2$  photoanode, the photoanode would like to create a stable equipotential interface and dynamic equilibrium between  $\text{MoS}_2\text{@TiO}_2$  photoanode surface and electrolyte. Due to the existing of  $\text{MoS}_2$  photocorrosion, the interface must re-establish itself after the photocorrosion of  $\text{MoS}_2$ , leading to photocharge fluctuations. This phenomenon was also observed for the 0.1 M  $\text{V}^{4+}$  concentration electrolyte (**Figure S9a, Supporting Information**). **Figure 6b** shows the discharge experiment after each full photocharge. Compared to the poor discharge performance (25.52  $\text{mAh L}^{-1}$  to 18.11  $\text{mAh L}^{-1}$ ) when using 0.1 M  $\text{V}^{4+}$  electrolyte (**Figure S9b, Supporting Information**), the much higher capacity (98.93  $\text{mAh L}^{-1}$  to 74.26  $\text{mAh L}^{-1}$ ) of 1.0 M  $\text{V}^{4+}$  (**Figure 6c**) can provide higher discharge potential to overcome the multiple resistances present in the system. The coulombic efficiency for 1.0 M and 0.1 M  $\text{V}^{4+}$  after five cycles is  $\sim 90\%$  (**Figure 7c**) and  $\sim 80\%$  (**Figure S9c, Supporting Information**), respectively. A SOC of 9.03% after 80 min of the

first photocharging cycle was observed, decreasing to 6.78% after 80 min into the fifth photocharging cycle.

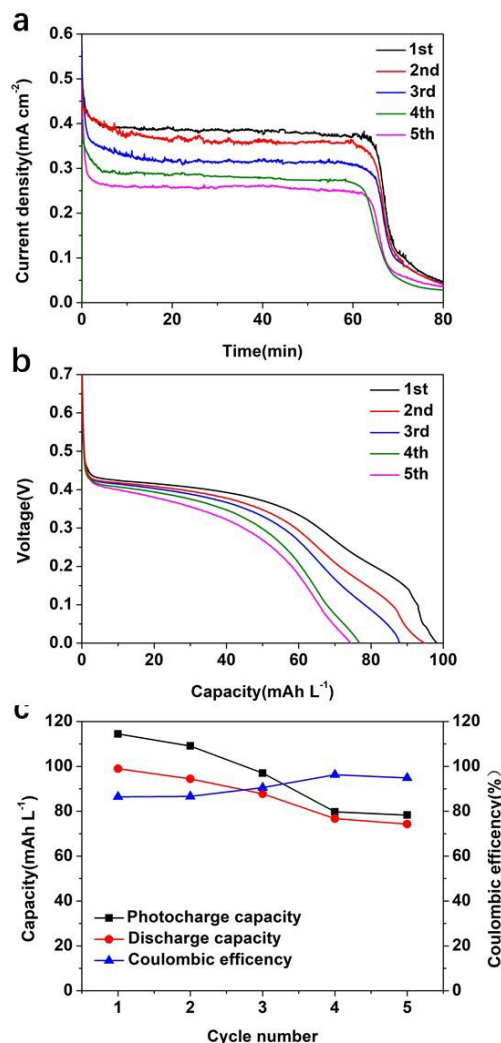
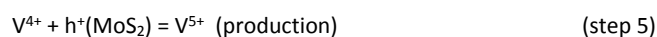
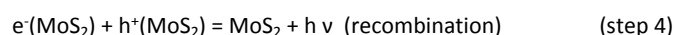
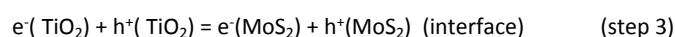
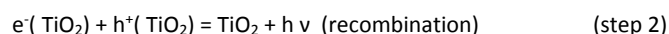
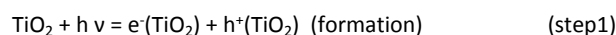


**Figure 6.** (a) Cyclic photocharge, (b) discharge of  $\text{MoS}_2\text{@TiO}_2\text{-}0.5$  and (c) the capacity and coulombic efficiency in the vanadium ion concentration of 1.0 M  $\text{V}^{4+}$ . The discharge current density is 0.4  $\text{mA cm}^{-2}$ . (100  $\text{mW cm}^{-2}$ (AG1.5) with 3.0 M  $\text{H}_2\text{SO}_4$  and 2.5 mL  $\text{min}^{-1}$  flow rate).

During photocharge process, the carriers from the semiconductor are excited to the conduction band and oxidise  $\text{V}^{4+}$  to  $\text{V}^{5+}$ . The photoexcitation and electron transfer can be represented as follows:



The average SOEE during photocharge in the SRFB was calculated according to the Equation 4<sup>44</sup>:

$$\text{SOEE (\%)} = (I_{\text{dis}} \times dt \times \Delta E_0) / (P_{\text{in}} \times S \times t) \times 100 \quad (4)$$

Where  $I_{\text{dis}}$  is the discharge current density,  $\Delta E_0$  is the potential difference of the two redox couples at reversible state,  $t$  is the illumination time (0.5 h or 1.33 h),  $P_{\text{in}}$  is the incident solar power ( $100 \text{ mW cm}^{-2}$ ), and  $S$  is the area of the solar flow cell window ( $5.0 \text{ cm}^2$ ).

As recorded in **Table 1**, the calculations showed the SOEE of the SRFB in  $1.0 \text{ M V}^{4+}$  reaches a value of 4.78% in the first cycle and remains at 3.26% in the fifth cycle.

Sample Cycle	0.1 M			1.0 M		
	Photocharge capacity (mAh L <sup>-1</sup> )	Discharge capacity (mAh L <sup>-1</sup> )	SOEE (%)	Photocharge capacity (mAh L <sup>-1</sup> )	Discharge capacity (mAh L <sup>-1</sup> )	SOEE (%)
1	32.68	25.52	0.17	114.44	98.93	4.78
2	26.23	22.50	0.14	109.09	94.47	4.31
3	23.92	21.00	0.12	96.99	87.79	3.99
4	21.38	18.69	0.11	79.72	76.74	3.49
5	21.28	18.11	0.09	78.29	74.26	3.26

**Table 1.** Dependence of SOEE from cycling chronoamperometry plot under illumination for the  $\text{MoS}_2/\text{TiO}_2$

EIS studies showed an increase in the impedance of  $\text{MoS}_2/\text{TiO}_2-0.5$  with photocharging (**Figure S10, Supporting Information**) reaching almost three times the initial value after 2 hours, revealing an increase in resistance as the photocharging process progresses, which was attributed to the low stability of the photoelectrode under strong acid electrolyte. This was confirmed via SEM images acquired after each cycle (**Figure S11, Supporting Information**). The SEM images clearly show degradation of the  $\text{MoS}_2$  layer upon cycling and suggest that the increase in resistance observed in the EIS may be linked to this degradation of  $\text{MoS}_2$ . The photoexcitation and electron transfer may be represented as shown in the Equation S1, Supporting Information.<sup>60</sup> The amounts of Mo and Ti leached from the photoanode were determined by ICP-MS and the results are shown in **Figure S12, Supporting Information**. The concentration of Mo in the electrolyte increases with the number of cycles, as expected, supporting the results obtained by SEM and EIS. The  $\text{TiO}_2$  layer was less affected by the cycling, but slight leaching was also detected for the  $1.0 \text{ M V}^{4+}$  electrolyte.

To understand the influence of the photoanode structure and to use its light absorption ability to effectively photocharge our solar flow cell, EIS was measured under both dark and light conditions for  $0.1$  and  $1.0 \text{ M V}^{4+}$  (**Figures 7a-d**). EIS data for  $\text{TiO}_2$  and  $\text{MoS}_2/\text{TiO}_2$  photoanodes both for low ( $0.1 \text{ M V}^{4+}$ ) and high electrolyte concentration ( $1.0 \text{ M V}^{4+}$ ) showed that the increase in thickness of the  $\text{TiO}_2$  leads to a decrease in impedance, effect that remains after adding the  $\text{MoS}_2$  layer. In the low frequency range in dark conditions, the mass transfer dominates the reaction for  $\text{TiO}_2-0.5$ .

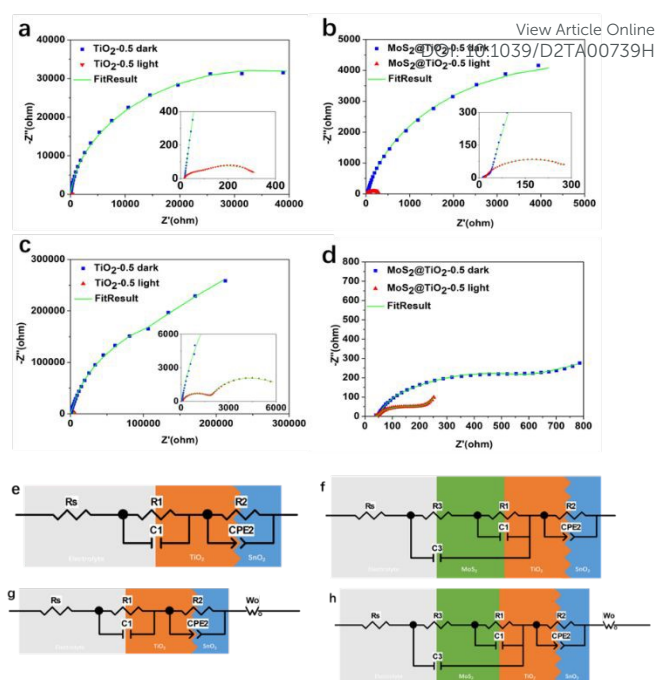


**Figure 7.** EIS of  $\text{TiO}_2-0.5$  or  $\text{MoS}_2/\text{TiO}_2-0.5$  as the working electrode under dark and light illumination ( $100 \text{ mW cm}^{-2}$ , AG1.5) in a three-electrode electrochemical cell using (a,b)  $0.1 \text{ M V}^{4+}$  or (c,d)  $1.0 \text{ M V}^{4+}$  in  $3.0 \text{ M H}_2\text{SO}_4$  as electrolyte and KCl saturated calomel  $\text{Hg}_2\text{Cl}_2$  electrode (SCE) and a Pt coil as reference and counter electrodes, respectively. Equivalent circuit model used to simulate the experimental data of (e)  $\text{TiO}_2-0.5$  and (f)  $\text{MoS}_2/\text{TiO}_2-0.5$  in  $0.1 \text{ M V}^{4+}$  and (g)  $\text{TiO}_2-0.5$  and (h)  $\text{MoS}_2/\text{TiO}_2-0.5$  in  $1.0 \text{ M V}^{4+}$ .

However, under illumination, the upward trend disappears, which means charge transfer dominates in that case (**Figure 7a, c**). For  $\text{MoS}_2/\text{TiO}_2-0.5$ , EIS results demonstrate that the addition of  $\text{MoS}_2$  to the  $\text{TiO}_2$  layer enhances the charge transfer properties of the photoelectrode (**Figure 7b, d**). Under illumination, the process remains dominated by mass transport effect for  $\text{MoS}_2/\text{TiO}_2-0.5$  photoanode at low frequencies, confirming its better performance compared to  $\text{TiO}_2-0.5$ . The equivalent circuits for  $\text{TiO}_2-0.5$  and  $\text{MoS}_2/\text{TiO}_2-0.5$  in  $0.1 \text{ M V}^{4+}$  (**Figure 7e, f**) exhibit slightly different interface components due to the differences in morphology and roughness of both photoelectrodes<sup>45</sup>. The EIS data taken in a three-electrode electrochemical cell and equivalent circuit for  $\text{TiO}_2/\text{FTO}$  and  $\text{MoS}_2/\text{TiO}_2/\text{FTO}$  systems show that at lower  $\text{V}^{4+}$  concentration, the diffusion resistance is also lower, because when the charge transfer dynamics are not very fast, the charge transfer process and the mass transfer process (caused by diffusion) control the overall reaction: electrochemical polarisation and concentration polarisation coexist. When the concentration is low, the charge transfer process is the rate-determining process. At higher concentration of  $\text{V}^{4+}$ , mass transport is introduced in the equivalent circuit as the Warburg impedance ( $W_0$  in the equivalent circuit, (**Figure 7g, h**), in addition to the charge transfer resistance, as there is an increase in diffusion resistance, when increasing concentration of  $\text{V}^{4+}$ .





The fitted data for the  $\text{TiO}_2$ -0.5 and  $\text{MoS}_2$ @ $\text{TiO}_2$ -0.5 photoelectrodes in 0.1 M  $\text{V}^{4+}$  and 1.0 M  $\text{V}^{4+}$  are consistent with the results obtained from both dark and light experiments.  $R_s$  represents the series resistance (resistance of electrolyte solution and cable of potentiostat),  $R_1$  and  $C_1$  represent the charge transfer resistance and capacitance of the electrolyte/ $\text{TiO}_2$  interface in  $\text{TiO}_2$ -0.5 while in  $\text{MoS}_2$ @ $\text{TiO}_2$ -0.5 they present  $\text{MoS}_2$ / $\text{TiO}_2$  interface,  $R_2$  and  $\text{CPE}_2$  represent the charge transfer equivalent structure of the interface between  $\text{SnO}_2$  (FTO) and  $\text{TiO}_2$ . In  $\text{MoS}_2$ @ $\text{TiO}_2$ -0.5, the  $R_1$  and  $C_1$  represent the impedance of  $\text{MoS}_2$ / $\text{TiO}_2$ . Because the  $\text{MoS}_2$  nanoflowers cannot form a dense layer to separate the  $\text{TiO}_2$  and the electrolyte,  $R_3$  and  $C_3$  is the collective effect representing the charge transfer resistance and capacitance of the electrolyte/ $\text{MoS}_2$  and electrolyte/ $\text{TiO}_2$  interfaces. The  $C_3$  element in parallel with  $R_1$ ,  $C_1$  and  $R_3$  is also associated with the same phenomenon. The main values of the circuit elements in dark and in light are listed in **Table 2**. The fitting models results of  $\text{TiO}_2$ -0.1/0.3 and  $\text{MoS}_2$ @ $\text{TiO}_2$ -0.1/0.3 in 0.1 M  $\text{V}^{4+}$  and 1.0 M  $\text{V}^{4+}$  fit well with the original data in **Figure S13, S14, Supporting Information**. The equivalent circuit is applicable for all the  $\text{TiO}_2$  and  $\text{MoS}_2$ @ $\text{TiO}_2$  combinations.

Table 2. Equivalent circuit main parameters of EIS.

Element		$R_3(\Omega)$	$C_3(\text{F})$	$R_1(\Omega)$	$C_1(\text{F})$	$R_2(\Omega)$	$\text{CPE}_2\text{-T}(\text{F})$	$\text{CPE}_2\text{-P}$
Sample								
0.1 M $\text{V}^{4+}$	$\text{TiO}_2$ -0.5 dark	N/A	N/A	1.7	$5.0 \times 10^{-6}$	70441	$1.9 \times 10^5$	0.9
	$\text{TiO}_2$ -0.5 light	N/A	N/A	32.9	$4.3 \times 10^{-5}$	297.3	$7.5 \times 10^4$	0.5
	$\text{MoS}_2$ @ $\text{TiO}_2$ -0.5 dark	6.6	$3.7 \times 10^{-6}$	13.4	$2.0 \times 10^{-5}$	10160	$1.9 \times 10^4$	0.8
	$\text{MoS}_2$ @ $\text{TiO}_2$ -0.5 light	3.1	$1.3 \times 10^{-5}$	23.9	$1.1 \times 10^{-3}$	291.3	$1.4 \times 10^3$	0.9
1.0 M $\text{V}^{4+}$	$\text{TiO}_2$ -0.5 dark	N/A	N/A	1921	$3.1 \times 10^{-6}$	$2.6 \times 10^5$	$1.4 \times 10^6$	0.9
	$\text{TiO}_2$ -0.5 light	N/A	N/A	2943	$1.4 \times 10^{-4}$	1776	$4.3 \times 10^{-6}$	0.8
	$\text{MoS}_2$ @ $\text{TiO}_2$ -0.5 dark	100.2	$9.3 \times 10^{-5}$	53.8	$3.4 \times 10^{-4}$	377.3	$5.4 \times 10^4$	0.8
	$\text{MoS}_2$ @ $\text{TiO}_2$ -0.5 light	40.5	$1.1 \times 10^{-4}$	19.3	$6.2 \times 10^{-4}$	30.9	$2.7 \times 10^3$	1.0

In dark conditions, due to the poor conductivity of the  $\text{TiO}_2$ , a large charge transfer resistance ( $R_{ct}$ ) is generated at the interface between  $\text{TiO}_2$  and  $\text{SnO}_2$  ( $\text{TiO}_2$ / $\text{SnO}_2$ ), hindering electron transport. In 0.1M  $\text{V}^{4+}$  and 1.0 M  $\text{V}^{4+}$ , under illumination, by comparing the sum of the charge transfer resistance of  $R_1+R_2+R_3$ , it is demonstrated that the introduction of  $\text{MoS}_2$  interface makes it easier for electrons to transfer in the photoanode, which makes the transmission of

the photogenerated electrons in the photoelectrode more efficient. In addition, the injection of photon significantly reduces the  $R_{ct}$  of the interface, especially in the  $\text{TiO}_2$ / $\text{SnO}_2$  interface. Due to the photon injection, many carriers are generated and moved to the interface ( $\text{MoS}_2$ / $\text{TiO}_2$ ,  $\text{TiO}_2$ / $\text{SnO}_2$ , electrolyte/ $\text{TiO}_2$  and electrolyte/ $\text{MoS}_2$ ). The enrichment of positive and negative charges on both sides of the interface increases the capacitance under illumination. By comparing the capacitance of  $\text{TiO}_2$  and  $\text{MoS}_2$ @ $\text{TiO}_2$ , it can be concluded that  $\text{MoS}_2$ @ $\text{TiO}_2$  exhibits more carriers accumulated at the interface, which also confirms that the heterojunction of  $\text{MoS}_2$ @ $\text{TiO}_2$  can effectively increase the carrier density in the photoanode.

## Conclusions

$\text{TiO}_2$  and  $\text{MoS}_2$ @ $\text{TiO}_2$  thin films supported on FTO were synthesised and tested as photoelectrodes in a solar redox flow battery using vanadium redox active species. Different thicknesses of  $\text{TiO}_2$  layer were produced. The results showed that a larger amount of Ti precursor resulted in more uniform, thicker, denser  $\text{TiO}_2$  thin film with more aligned  $\text{TiO}_2$  rods. This, in turn, led to a more efficient attachment of the  $\text{MoS}_2$  nanoflower overlayer that also translated into a higher photocurrent response. The designed  $\text{MoS}_2$ @ $\text{TiO}_2$  photoelectrode exhibited around 5 times higher activity than bare  $\text{TiO}_2$  for charging the all-V SRFB tested in this work. This was attributed to a better separation of charge carriers. The SRFB with 1.0 M  $\text{V}^{4+}$  electrolyte exhibited a remarkable performance, with an average capacity of 1077 mAh  $\text{L}^{-1}$  and coulombic efficiency of 99.2% at a current density of 1.0 mA  $\text{cm}^{-2}$  within 25 cycles, charged only by solar energy without the need of any bias. The SOEE attained 4.78% efficiency. The photoelectrode interfaces were analysed in detail through EIS, and successfully confirmed the enhancement of photocurrent response with the addition of the  $\text{MoS}_2$  layer to the  $\text{TiO}_2$  photoelectrode. This indicates that the highly active  $\text{MoS}_2$ @ $\text{TiO}_2$  photoanode is promising for the enhancement of photocurrent density in the system studied. The  $\text{MoS}_2$  facilitated charge carrier separation and provided active sites for oxidation of redox species. However, the low stability of the photoanode under strong acidic conditions led to a significant degradation of the photoelectrode after only five cycles, resulting in the leaching of metal to the electrolyte. More research is currently under way into approaches to protect the photoelectrode against degradation.

## Author Contributions

GT: investigation, formal analysis, methodology, visualisation, writing-original draft and editing. RJ: formal analysis, writing and editing. JB: writing and editing. MT: writing and editing. AJS: conceptualisation, formal analysis, resources, funding acquisition, writing and editing.



## Conflicts of interest

There are no conflicts to declare.

## Acknowledgements

The authors acknowledge Dr. Ryan Wang, Jay Yan, Zhangyi Yao, Junrun Feng and Yue Wen at UCL Department of Chemical Engineering for their help with the ICP measurements. GT acknowledges his PhD scholarship funded by the Chinese Scholarship Council, AJS thanks her UKRI Future Leaders Fellowship (MR/T041412/1) for funding support.

## Notes and references

- Yan, N., Li, G. and Gao, X. *Journal of Materials Chemistry A*, 2013, **1**, 7012-7015.
- Khataee, A., Azevedo, J., Dias, P., Ivanou, D., Dražević, E., Bontien, A. and Mendes, A. *Nano Energy*, 2019, **62**, 832-843.
- Skyllas-Kazacos, M., Rychcik, M., Robins, R. G., Fane, A. and Green, M. *Journal of the electrochemical society*, 1986, **133**, 1057.
- Skyllas-Kazacos, M., Chakrabarti, M., Hajimolana, S., Mjalli, F. and Saleem, M. *Journal of the electrochemical society*, 2011, **158**, R55.
- Vázquez-Galván, J., Flox, C., Jervis, J., Jorge, A., Shearing, P. and Morante, J. *Carbon*, 2019, **148**, 91-104.
- Delgado, N. M., Monteiro, R. and Mendes, A. *Nano Energy*, 2021, 106372.
- Feng, H., Jiao, X., Chen, R., Zhu, X., Liao, Q., Ye, D., Zhang, B. and Zhang, W. *Journal of Power Sources*, 2019, **419**, 162-170.
- Wei, Z., Almakrami, H., Lin, G., Agar, E. and Liu, F. *Electrochimica Acta*, 2018, **263**, 570-575.
- Fujishima, A., Rao, T. N. and Tryk, D. A. *Journal of photochemistry and photobiology C: Photochemistry reviews*, 2000, **1**, 1-21.
- Cui, H., Zhao, W., Yang, C., Yin, H., Lin, T., Shan, Y., Xie, Y., Gu, H. and Huang, F. *Journal of Materials Chemistry A*, 2014, **2**, 8612-8616.
- Butburee, T., Bai, Y., Wang, H., Chen, H., Wang, Z., Liu, G., Zou, J., Khemthong, P., Lu, G. Q. M. and Wang, L. *Adv Mater*, 2018, **30**, e1705666.
- Fujishima, A. and Honda, K. *nature*, 1972, **238**, 37-38.
- Nakata, K. and Fujishima, A. *Journal of photochemistry and photobiology C: Photochemistry Reviews*, 2012, **13**, 169-189.
- Akpan, U. and Hameed, B. *Applied Catalysis A: General*, 2010, **375**, 1-11.
- Ohno, T., Mitsui, T. and Matsumura, M. *Chemistry letters*, 2003, **32**, 364-365.
- Subramanian, V., Wolf, E. E. and Kamat, P. V. *J Am Chem Soc*, 2004, **126**, 4943-50.
- Zheng, Z., Huang, B., Qin, X., Zhang, X., Dai, Y. and Whangbo, M.-H. *Journal of Materials Chemistry*, 2011, **21**, 9079-9087.
- Gao, C., Wei, T., Zhang, Y., Song, X., Huan, Y., Liu, H., Zhao, M., Yu, J. and Chen, X. *Adv Mater*, 2019, **31**, e1806596.
- Humayun, M., Raziq, F., Khan, A. and Luo, W. *Green Chemistry Letters and Reviews*, 2018, **11**, 86-102.
- Bessekhouad, Y., Robert, D. and Weber, J.-V. *Catalysis today*, 2005, **101**, 315-321.
- Low, J., Yu, J., Jaroniec, M., Wageh, S. and Al-Ghamdi, A. A. *Adv Mater*, 2017, **29**, 1601694.
- Sotelo-Vazquez, C., Quesada-Cabrera, R., Ling, M., Scanlon, D. O., Kafizas, A., Thakur, P. K., Lee, T. L., Taylor, A., Watson, G. W. and Palgrave, R. G. *Advanced Functional Materials*, 2017, **27**, 1605413.
- Wang, H., Zhang, L., Chen, Z., Hu, J., Li, S., Wang, Z., Liu, J. and Wang, X. *Chem Soc Rev*, 2014, **43**, 5234-44.
- Li, J., Zhang, M., Li, X., Li, Q. and Yang, J. *Applied Catalysis B: Environmental*, 2017, **212**, 106-114.
- Yuan, N., Zhang, J., Zhang, S., Chen, G., Meng, S., Fan, Y., Zheng, X. and Chen, S. *The Journal of Physical Chemistry C*, 2020, **124**, 8561-8575.
- Cheng, B. Y., Yang, J. S., Cho, H. W. and Wu, J. J. *ACS Appl Mater Interfaces*, 2016, **8**, 20032-9.
- Alcudia-Ramos, M., Fuentez-Torres, M., Ortiz-Chi, F., Espinosa-González, C., Hernández-Como, N., García-Zaleta, D., Kesarla, M., Torres-Torres, J., Collins-Martínez, V. and Godavarthi, S. *Ceramics International*, 2020, **46**, 38-45. DOI: 10.1039/B27A00789H
- He, H., Lin, J., Fu, W., Wang, X., Wang, H., Zeng, Q., Gu, Q., Li, Y., Yan, C. and Tay, B. K. *Advanced Energy Materials*, 2016, **6**, 1600464.
- Yang, L., Majumdar, K., Liu, H., Du, Y., Wu, H., Hatzistergos, M., Hung, P. Y., Tieckelmann, R., Tsai, W., Hobbs, C. and Ye, P. D. *Nano Lett*, 2014, **14**, 6275-80.
- Li, W., Fu, H. C., Li, L., Caban-Acevedo, M., He, J. H. and Jin, S. *Angew Chem Int Ed Engl*, 2016, **55**, 13104-13108.
- Cheng, Q., Fan, W., He, Y., Ma, P., Vanka, S., Fan, S., Mi, Z. and Wang, D. *Advanced Materials*, 2017, **29**, 1700312.
- Liu, Y., Li, Y., Peng, F., Lin, Y., Yang, S., Zhang, S., Wang, H., Cao, Y. and Yu, H. *Applied Catalysis B: Environmental*, 2019, **241**, 236-245.
- Ribadeneyra, M. C., Grogan, L., Au, H., Schlee, P., Herou, S., Neville, T., Cullen, P. L., Kok, M. D., Hosseinaei, O. and Danielsson, S. *Carbon*, 2020, **157**, 847-856.
- Wang, D., Xu, Y., Sun, F., Zhang, Q., Wang, P. and Wang, X. *Applied Surface Science*, 2016, **377**, 221-227.
- Liu, C., Wang, L., Tang, Y., Luo, S., Liu, Y., Zhang, S., Zeng, Y. and Xu, Y. *Applied Catalysis B: Environmental*, 2015, **164**, 1-9.
- Geng, X., Sun, W., Wu, W., Chen, B., Al-Hilo, A., Benamara, M., Zhu, H., Watanabe, F., Cui, J. and Chen, T. P. *Nat Commun*, 2016, **7**, 10672.
- Chang, K., Hai, X., Pang, H., Zhang, H., Shi, L., Liu, G., Liu, H., Zhao, G., Li, M. and Ye, J. *Adv Mater*, 2016, **28**, 10033-10041.
- Zhou, X., Lickleder, M. and Schmuki, P. *Electrochemistry Communications*, 2016, **73**, 33-37.
- Liu, H., Lv, T., Zhu, C., Su, X. and Zhu, Z. *Journal of Molecular Catalysis A: Chemical*, 2015, **396**, 136-142.
- Vrubel, H., Merki, D. and Hu, X. *Energy & Environmental Science*, 2012, **5**, 6136-6144.
- Sun, M., Wang, Y., Fang, Y., Sun, S. and Yu, Z. *Journal of Alloys and Compounds*, 2016, **684**, 335-341.
- Wang, W. and Wang, X. *Electrochimica Acta*, 2007, **52**, 6755-6762.
- Ulaganathan, M., Jain, A., Aravindan, V., Jayaraman, S., Ling, W. C., Lim, T. M., Srinivasan, M. P., Yan, Q. and Madhavi, S. *Journal of Power Sources*, 2015, **274**, 846-850.
- Liao, S., Zong, X., Seger, B., Pedersen, T., Yao, T., Ding, C., Shi, J., Chen, J. and Li, C. *Nat Commun*, 2016, **7**, 11474.
- Fakhr Nabavi, H. and Aliofkhae, M. *Surface and Coatings Technology*, 2019, **375**, 266-291.

